

Efficient and stable blue quantum dot light-emitting diode

<https://doi.org/10.1038/s41586-020-2791-x>

Received: 9 May 2020

Accepted: 21 August 2020

Published online: 14 October 2020

 Check for updates

Taehyung Kim¹, Kwang-Hee Kim¹, Sungwoo Kim¹, Seon-Myeong Choi¹, Hyosook Jang¹, Hong-Kyu Seo¹, Heejae Lee¹, Dae-Young Chung¹ & Eunjoo Jang¹✉

The visualization of accurate colour information using quantum dots has been explored for decades, and commercial products employing environmentally friendly materials are currently available as backlights¹. However, next-generation electroluminescent displays based on quantum dots require the development of an efficient and stable cadmium-free blue-light-emitting device, which has remained a challenge because of the inferior photophysical properties of blue-light-emitting materials^{2,3}. Here we present the synthesis of ZnSe-based blue-light-emitting quantum dots with a quantum yield of unity. We found that hydrofluoric acid and zinc chloride additives are effective at enhancing luminescence efficiency by eliminating stacking faults in the ZnSe crystalline structure. In addition, chloride passivation through liquid or solid ligand exchange leads to slow radiative recombination, high thermal stability and efficient charge-transport properties. We constructed double quantum dot emitting layers with gradient chloride content in a light-emitting diode to facilitate hole transport, and the resulting device showed an efficiency at the theoretical limit, high brightness and long operational lifetime. We anticipate that our efficient and stable blue quantum dot light-emitting devices can facilitate the development of electroluminescent full-colour displays using quantum dots.

Ever since the quantum dot light-emitting diode (QD-LED) was suggested as an ideal display⁴, continuous efforts have been devoted to improving its performance^{2,3}. The external quantum efficiencies (EQEs) of state-of-the-art red, green and blue QD-LEDs are 20.5% (ref. ⁵), 23.9% (ref. ⁶) and 19.8% (ref. ⁷), respectively, which are regarded as the theoretical limits considering light out-couplings. In terms of operational lifetime, red and green QD-LEDs have shown sufficient lifetimes of $T_{95} = 3,800$ h (ref. ⁸) and $T_{95} = 2,500$ h (ref. ⁶), respectively, but the stability of blue QD-LEDs is much poorer⁸ (T_{95} , time for the brightness to decrease to 95% of the initial value). Previous studies suggested that the causes of the short lifetime are non-radiative recombination⁹, built-up charge at the QD–electron transport layer (ETL) interface¹⁰ and instability of ligands under an electric bias⁸. Another critical issue is the toxicity of cadmium¹, which is a severe obstacle to commercialization. Recently, environmentally friendly InP-based red QD-LEDs showed comparable performances to Cd-based QD-LEDs in terms of EQE (21.4%) and lifetime ($T_{95} = 615$ h at $1,000$ cd m^{-2})¹¹. However, the best-controlled emission wavelength of InP was too long to be a blue emitter, and the highest photoluminescence quantum yield was only 76% (ref. ¹²). InP/GaP/ZnS QDs showed a photoluminescence quantum yield of 81% at 480 nm with a low EQE of ~1% (ref. ¹³). ZnSe-based QDs have been investigated as a potential Cd-free blue emitter^{14,15}. Recently, ZnTeSe QD-LEDs showed EQE = 4.2% with a short lifetime ($T_{50} = 5$ min at 200 cd m^{-2} ; T_{50} , time required for the brightness to decrease to 50% of the initial value)¹⁶, and the same authors reported an improved EQE of up to 9.5%, but without stability, by using modified ETLs¹⁷. Here, we present a method for the preparation of efficient blue ZnTeSe/ZnSe/

ZnS QDs. The emission wavelength is tuned at 457 nm by Te doping, and the photoluminescence quantum yield is improved by up to 100% by removing stacking faults and passivating surface-dangling defects with chlorides. In addition, further Cl^- treatment replaces native aliphatic ligands to improve thermal stability and charge injection/transport. Moreover, the emitting layer (EML) is designed as double stacks with a gradient Cl concentration for efficient charge recombination. The resulting device shows an EQE of up to 20.2% with a brightness of $88,900$ cd m^{-2} , and $T_{50} = 15,850$ h at 100 cd m^{-2} , which are the highest values reported so far for blue QD-LEDs.

Figure 1a summarizes the synthetic scheme used to prepare ZnTeSe core, ZnTeSe/ZnSe core/shell (C/S) and ZnTeSe/ZnSe/ZnS core/shell/shell (C/S/S) QDs, including transmission electron microscopy (TEM) images. The Te/Se ratio was determined as 6.7 mol% in the core (diameter, 3.1 nm) to tune the emission wavelength in the blue region (457 nm). The thicknesses of the ZnSe and the ZnS shells were 2.6 nm and 1.2 nm, respectively, and their elemental compositions were analysed using inductively coupled plasma atomic emission spectroscopy (ICP-AES). The emission wavelengths as a function of the Te concentration, core size and ZnSe thickness were also calculated with the effective mass approximation (Extended Data Fig. 1d–f). The size distributions of the core, C/S and C/S/S QDs appear to be less than 10%, and the C/S/S QDs have a cubic shape showing zinc blende structures (Extended Data Fig. 1). As the ZnSe shell evolves, stacking faults are easily generated; these are most clearly shown as a hazy pattern between the (022) and (113) diffraction planes in high-resolution TEM (Fig. 1b), and also as broadened shoulder peaks in the X-ray powder diffraction (XRD) image

¹Samsung Advanced Institute of Technology, Samsung Electronics, Suwon, Republic of Korea. ✉e-mail: ejjang12@samsung.com

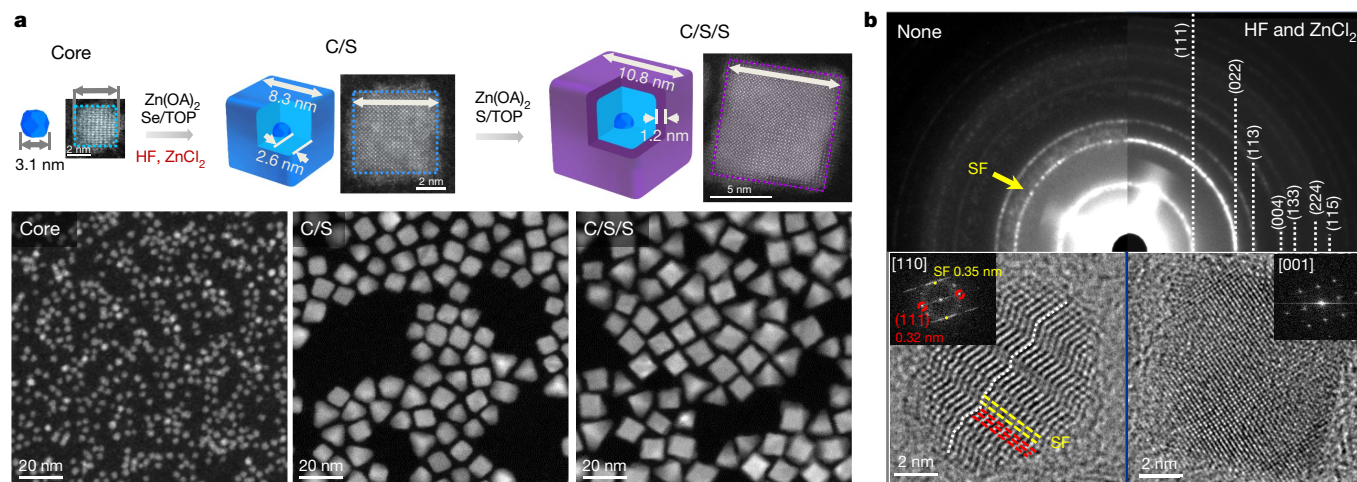


Fig. 1 | Characterization of ZnTeSe/ZnSe/ZnS QDs. **a**, Schematic illustrations of the synthesis of ZnTeSe (core), ZnTeSe/ZnSe (C/S) and ZnTeSe/ZnSe/ZnS (C/S/S) QDs, with corresponding TEM images. The chemical compositions (atomic ratios) measured with ICP-AES are: core (Zn:Te:Se = 0.571:0.027:0.4), C/S (Zn:Te:Se = 0.521:0.002:0.476), C/S/S (Zn:Te:Se:S = 0.528:0.001:0.255:0.215). **b**, Selected-area diffraction (SAED) patterns for two types of C/S/S QDs (top) and

corresponding high-resolution TEM images of a single particle (bottom), prepared without additives ('None', left) and prepared with HF and ZnCl₂ ('HF and ZnCl₂', right). Yellow dotted lines indicate the locations of stacking faults (SF) and red dotted lines show the normal zinc blende crystalline layer. Insets, diffraction patterns measured along the [110] and [001] axes.

(Extended Data Fig. 2a). The original lattice distance of the (111) surface is 0.32 nm, but the stacking fault has a larger distance of 0.35 nm, corresponding to the shoulder at 26° (smaller than the diffraction angle of 27° of the (111) peak). Orfield et al.¹⁸ also reported that stacking faults of CdSe/CdS QDs facilitate non-radiative recombination. Similarly, our C/S/S QDs contained many stacking faults before the optimization and showed a poor photoluminescence quantum yield of 50% (Extended Data Fig. 2). Suspecting that stacking faults were caused by steric hindrances from bulky aliphatic ligands, we added ZnCl₂ and hydrofluoric acid (HF) during the shell growth. The ZnCl₂ was able to replace the bulky ligand, resulting in a photoluminescence quantum yield of up to 77%. In addition, HF was able to detach the ligand by protonation, but exposed surfaces developed oxidized states, which were effectively etched out by HF. As a result, stacking faults were reduced remarkably, and the photoluminescence quantum yield was enhanced up to 70%. We employed halides at the early stage of ZnSe shell growth to control the growth directions because it was expected that halides could effectively stabilize certain facets. Indeed, ZnCl₂ induced the development of edged structures with well defined (100) or (111) facets. The high photoluminescence quantum yields of the QDs prepared with HF or ZnCl₂ are also reflected by the longer decay times in the time-resolved photoluminescence (TR-PL) spectra (Extended Data Fig. 2d). The addition of HF increased the average decay time (τ) from 26.4 ns to 43.4 ns by suppressing fast decay components. Meanwhile, ZnCl₂ induced an additional slow decay mode and the overall τ was increased to 77 ns, implying that Cl⁻ passivation created a pathway other than band-edge transition. When we used both HF and ZnCl₂ during the shell growth, stacking faults were almost completely removed, resulting in an enhanced photoluminescence quantum yield of 93%. However, the spectral width of current C/S/S QDs was rather broad (full width at half-maximum, 36 nm), which was caused by delocalized hole traps due to heterogeneous Te incorporation^{19,20} and the energy levels of the Cl⁻-passivated surfaces²¹. The effect of the Te concentration on the optical properties and the schematic energy diagram are shown in Extended Data Fig. 2e–g.

Before using C/S/S QDs in LEDs, native oleic acid (OA) ligand was replaced with ZnCl₂ through two steps of ligand exchange: a liquid-phase treatment (denoted as C/S/S-Cl(l)) and a film-washing treatment (C/S/S-Cl(f)) (Fig. 2a). Because ZnCl₂ provides better passivation of surface defects than OA, C/S/S-Cl(l) QDs showed a photoluminescence

quantum yield of 100% (Fig. 2b), and the Tr-PL spectrum reveals that the decay time increased to 67.4 ns (Extended Data Fig. 3a). To understand the microscopic origins of Cl⁻ passivation, we used density functional theory (DFT) to calculate the binding energies of the acetate ion (Ac⁻; a representative carboxylic acid) and the Cl⁻ ion on the ZnS surface (Fig. 2c). We assumed that only Zn atoms are exposed on the (100) surface of a cubic structure, based on the Zn-to-chalcogenide ratio obtained from ICP-AES. Our calculation showed that anions bound to Zn dangling bonds stabilized the surface energy, and that the Cl⁻ ligand was favoured over Ac⁻ for all possible coordinations (Extended Data Fig. 4). Because each Zn atom has two dangling bonds with 0.5 electrons, it binds to one anionic ligand for full passivation, with the formation of either a monodentate or a bidentate bridge. As the Ac⁻ ligand coverage exceeds 50%, the binding energy starts to decrease owing to steric hindrances. Previous studies showed similar trends^{22,23}, with halides passivating cramped sites better than bulky ligands. In addition, the density of states indicates that mid-gap trap states near the valence band maximum in under-passivated surfaces (Ac₂/Zn₄) are eliminated by the additional Cl (Ac₂Cl₂/Zn₄) (Fig. 2d), which explains the improvement in photoluminescence quantum yield after ligand exchange. Furthermore, because the spectral width and the radiative decay time increased, we suspected that the Cl passivation potentially contributed to changes in energy transitions²¹. Thermogravimetric analysis (TGA) indicates that the amount of the initial OA ligand on C/S/S QDs was 11.3 wt%, which corresponds to 19% of the surface Zn atoms (Extended Data Table 1). Because our optimized structure in the DFT calculation shows that Zn atoms have bidentate coordinations with OA, which is also supported by Fourier transform infrared spectroscopy (FT-IR; Extended Data Fig. 3e), 38% of the surface Zn can coordinate to OA (OA₂/Zn₄). After ligand exchange with ZnCl₂, the amount of coordinated OA to Zn atoms was reduced to 24%, and Cl could combine with another 68% of Zn atoms based on the Cl/Zn ratio obtained from X-ray photoemission spectroscopy (XPS). However, when ZnCl₂ removes OA excessively, QDs tend to aggregate in the solution, which can be detected by dynamic light-scattering (DLS) measurements (Extended Data Fig. 3f–h). Therefore, we prepared a C/S/S-Cl(l) film and washed it with ZnCl₂ solution to strip residual OA and produce a C/S/S-Cl(f) film. The photoluminescence properties are maintained after the film-washing treatment (Extended Data Fig. 3b, c). The carbon contents from XPS and the characteristic vibrations of

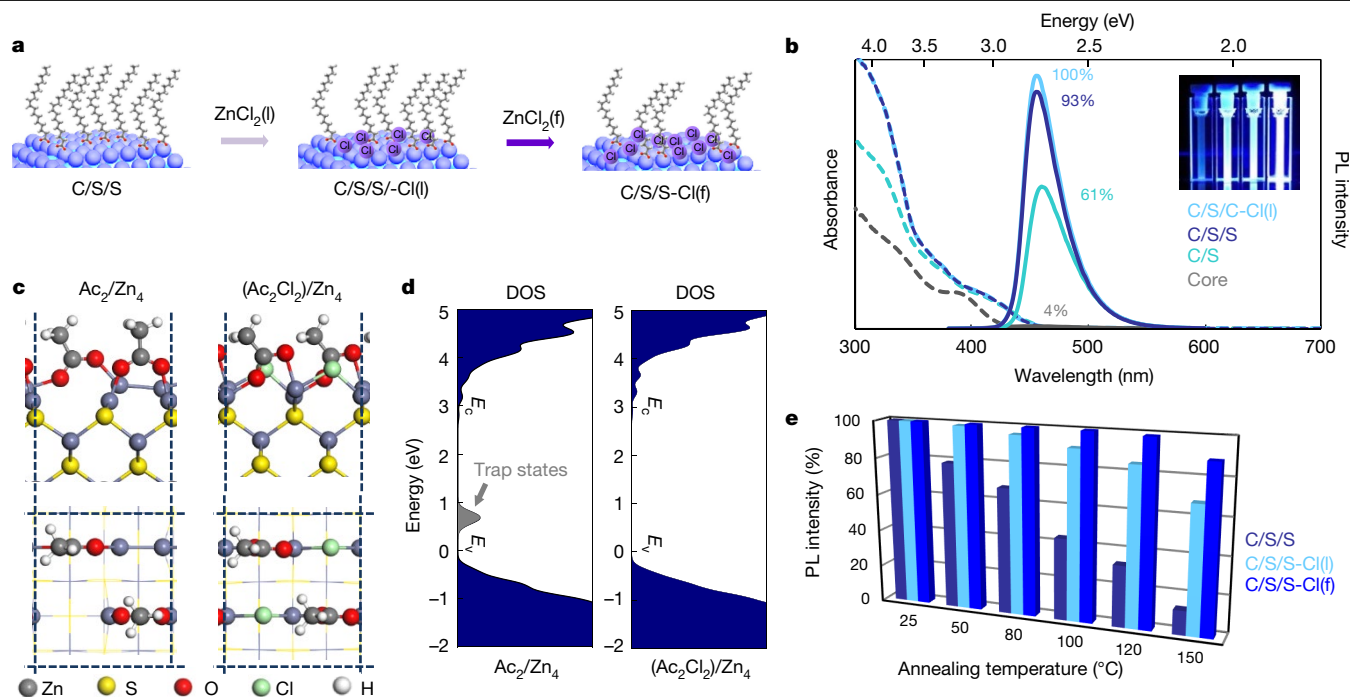


Fig. 2 | Chloride passivation of surface defects. **a**, Schematic drawing of the ligand exchange with ZnCl_2 in the liquid phase ($\text{ZnCl}_2(\text{l})$) and further exchange through film-washing treatment ($\text{ZnCl}_2(\text{f})$). **b**, Absorption and photoluminescence (PL) spectra of the QDs. Inset, photograph taken under illumination at 365 nm; from left to right: core, C/S, C/S/S and C/S/S-Cl(l). **c**, Relaxed configurations of

ZnS (100) surfaces with ligands for the under-passivated (Ac_2/Zn_4) and the fully passivated ($\text{Ac}_2\text{Cl}_2/\text{Zn}_4$) states. **d**, Calculated density of states (DOS) for Ac_2/Zn_4 and (Ac_2Cl_2)/ Zn_4 surfaces. E_v , valence band maximum; E_c , conduction band minimum. **e**, Dependence of photoluminescence stability of QD films on the annealing temperature. a.u., arbitrary units.

COO^- in the FT-IR data ($1,545\text{ cm}^{-1}$ and $1,403\text{ cm}^{-1}$) showed that about half of OA was removed from C/S/S-Cl(l) during the solid-state exchange. The elemental ratio Cl/Zn increased from 0.1 to 0.18, which is equivalent to 119% of bidentate Zn coordination (Extended Data Table 1). We also noticed that the thermal stability of the Cl^- -passivated QD films improved remarkably. Whereas the C/S/S QD film retained only 19% of the initial photoluminescence intensity after baking at $150\text{ }^\circ\text{C}$, the Cl^- -passivated C/S/S-Cl(l) and C/S/S-Cl(f) films kept 76% and 90% of the initial photoluminescence, respectively (Fig. 2e), because of the strong Cl^- binding²⁴.

Small inorganic ligands are also advantageous for charge injection/transport in QD photovoltaics and transistors^{25,26}. However, most existing QD-LEDs use native organic ligands to maintain the luminescence efficiency. Previous studies on ligand-exchange QD-LEDs have reported that replacing OA with octanethiol in ZnCdS/ZnS QDs enhanced the EQE 1.7 times²⁷, and the use of electrochemically inert amine ligand in CdSe/CdS QDs extended the lifetimes of red- and blue-emitting LEDs by up to $T_{95} = 3,800\text{ h}$ at $1,000\text{ cd m}^{-2}$ and $T_{50} = 10,000\text{ h}$ at 100 cd m^{-2} , respectively⁸. Recently, Li et al. applied thionylchloride to green-emitting QD-LEDs and obtained the highest so far brightness of $460,000\text{ cd m}^{-2}$ by enhancing the charge density. However, the authors reported an EQE of 6.4% without a lifetime test²⁸. We fabricated a QD-LED with a double EML consisting of C/S/S-Cl(l) and C/S/S-Cl(f) layers to improve charge injection/transport and recombination simultaneously. A schematic of the device structure is shown in Fig. 3a, including the energy levels for each layer. In the double EML, C/S/S-Cl(f) with the smallest amount of OA was used as the bottom layer for efficient hole transport. Compared to the QD-LED with pristine C/S/S, the current density of the QD-LEDs with C/S/S-Cl(f) increased 200 times at 3.5 V, and the turn-on voltage decreased to 2.6 V. We believe that the hole injection became more facile because of the OA removal, even though the valence band maximum measured with photoelectron spectroscopy deepens from -5.5 eV to -6.0 eV as the amount of Cl increases (Extended Data Fig. 5a, b). Besides,

the low conduction band minimum of C/S/S-Cl(f) allows easy access of electrons from the ZnMgO ETL. The QD-LEDs with C/S/S, C/S/S-Cl(l) and C/S/S-Cl(f) showed a brightness of $25,000\text{ cd m}^{-2}$, $40,120\text{ cd m}^{-2}$ and $68,220\text{ cd m}^{-2}$ and EQEs of 8.0%, 10.2% and 14.3%, respectively. The improvements in EQE and brightness agree well with the photoluminescence trends observed after thermal annealing of each QD. During the spin-coating of the double EML, the bottom layer retained 97% of the initial thickness after the ZnCl_2 washing treatment, and the subsequent top layer coating maintained uniform morphology (Extended Data Fig. 5c–e). The depth profile of the Cl^- content in the double EML was measured using TEM energy-dispersive X-ray spectroscopy (EDX) (Fig. 3b, Extended Data Fig. 5f, g). Our optimized device showed considerable improvements in both efficiency and brightness of up to 20.2% and $88,900\text{ cd m}^{-2}$, respectively. To check the reproducibility, we prepared 90 devices with the same structure, which displayed an average EQE of 17.0% and average brightness of $72,873\text{ cd m}^{-2}$ (Extended Data Fig. 6a, b). The operational stability was improved remarkably; T_{50} was measured as 442 h at the initial brightness of 650 cd m^{-2} (Fig. 3f), which was equivalent to 15,850 h at 100 cd m^{-2} according to the empirical acceleration factor of 1.9 (Extended Data Fig. 6d). These are outstanding performances compared to those of previously reported blue QD-LEDs, including Cd-based ones (Extended Data Table 2).

To elucidate the effect of the Cl^- passivation on the QD-LEDs, we prepared single-carrier devices (Fig. 4a), which showed that both the electron and hole currents increased substantially after the Cl^- passivation. Fittings with a space-charge-limited current model indicate that the hole mobility increased by an order of magnitude after the Cl^- passivation. Because the electron mobility still increased, but much less than that of the holes (Extended Data Fig. 7a–f), the differences in the electron and hole mobilities could be resolved by Cl^- passivation. Mott–Schottky analysis (Extended Data Fig. 7g, h) confirmed that the flat-band potentials in hole-only devices (HODs) and electron-only devices (EODs) changed similarly. To probe the recombination zone, we

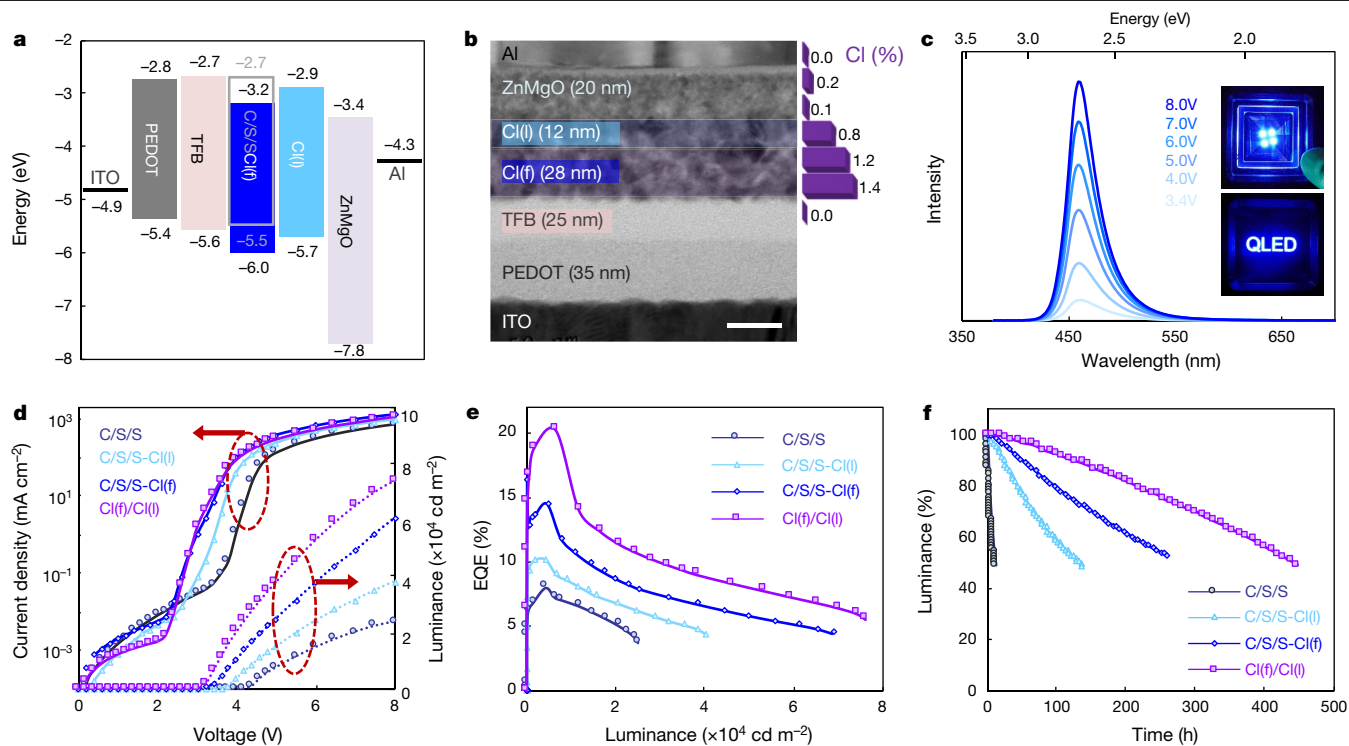


Fig. 3 | Performance of QD-LEDs. **a**, Energy-band diagram of the QD-LEDs. The grey square indicates the energy level of the C/S/S-OA QD before chlorination. **b**, Cross-sectional TEM image (scale bar, 30 nm) of the QD-LED with double EML. The vertical concentration of Cl was measured using high-resolution TEM EDX (Extended Data Fig. 5e, f). **c**, Voltage-dependent electroluminescence

spectra of the QD-LED with double EML. Inset, photographs of the operating devices. **d**, Voltage-dependent current density (left axis) and luminance (right axis). **e**, Luminance dependence of the EQE. **f**, Operation lifetime of the QD-LEDs measured at the initial brightness of 650 cd m^{-2} .

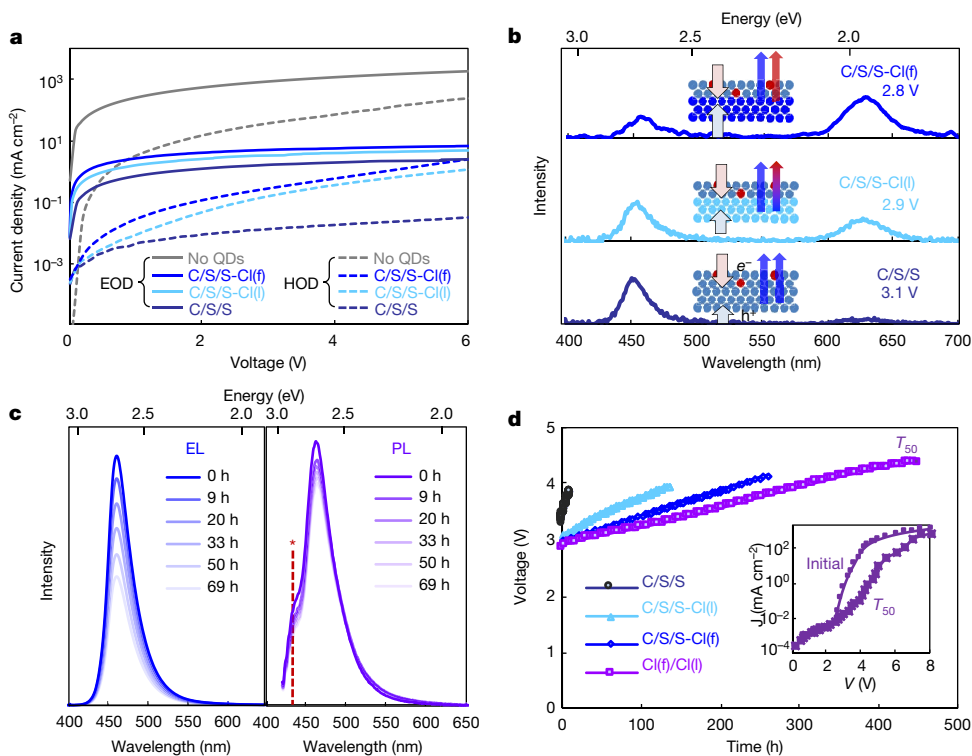


Fig. 4 | Analysis of device characteristics. **a**, Current density (J)–voltage (V) characteristics of EODs and HODs with no QDs, C/S/S, C/S/S-Cl(i) and C/S/S-Cl(f) QDs. **b**, Electroluminescence (EL) spectra of QD-LEDs with the top EML containing red-emitting QDs and various bottom EMLs: C/S/S, C/S/S-Cl(i) and C/S/S-Cl(f). **c**, Time-dependent electroluminescence and photoluminescence

spectra measured from a QD-LED with double EML at an initial brightness of $2,000 \text{ cd m}^{-2}$. The asterisk marks the emission from the HTL. **d**, Voltage change during the operation of the QD-LEDs. Inset, J – V profiles of the QD-LED with double EML before (initial) and after (T_{50}) operation.

prepared a double EML with a top layer doped with 5% red-emitting InP/ZnSe/ZnS QDs¹¹. Stronger red emission was observed near the turn-on voltage, as the bottom layer contained more Cl (Fig. 4b, Extended Data Fig. 8a–c). This reveals that charges recombine at the hole-transport layer (HTL)–EML interface when the holes are slow, and the recombination zone moves into the EML as the holes become faster. Therefore, we could confine the recombination zone inside the QD EML by controlling the Cl concentration. Because the operational lifetime of blue QD-LEDs is still lower than those of red or green devices, we compared the photoluminescence and electroluminescence intensities from the QD-LED to investigate the degradation mechanism. When the electroluminescence decreased to 50%, the photoluminescence still maintained more than 85% of its initial intensity (Fig. 4c). Therefore, the internal quantum yield drop might not be the origin of the short lifetime. We also found that the driving voltage increased during operation, and that this increase was alleviated by the Cl[−] passivation (Fig. 4d). This led us to suspect that the depletion of the TFB (see Methods) or ZnMgO layer could be more responsible for our device failure than the QD EML. A previous study suggested that the deterioration of the ZnO ETL is the main reason, because of the high electron-injection barrier against QDs¹⁰. When we compared the current–voltage profiles before and after the lifetime test (Fig. 4d inset), we observed a distinctive drop in the current density over the entire voltage range. Dynamic modulus plots obtained by impedance spectroscopy^{29,30} showed that the carrier injection was retarded after operation; the capacitive semi-circle remained at high voltages, and the deviation from the initial state appeared in the high-frequency regime. This implies that the degradation associated with the ZnMgO ETL (Extended Data Fig. 8d) is the biggest cause for the inferior stability of the blue QD-LEDs. Furthermore, the increased resistance caused by the deterioration of the ETL could make the QDs experience highly charged states.

In summary, the amount of Te doping in the core was tuned for perfect blue emission at 457 nm. A high photoluminescence quantum yield of 93% was obtained for the ZnTeSe/ZnSe/ZnS QD by using HF and ZnCl₂, and additional Cl[−] passivation through a ligand-exchange process improved the photoluminescence quantum yield of the C/S/S QD to 100%. Solid-state exchange with ZnCl₂ made the QDs thermally robust and conductive. In addition, a DFT calculation of the surface ligands revealed that Cl binds more strongly than OA and removes traps by passivating dangling bonds. The Cl[−] passivation improves charge transport considerably, so that the EQE and the brightness of the QD-LEDs are substantially enhanced. Moreover, our optimized blue QD-LED with double EML showed an EQE close to the theoretical limit (20.2%) and a brightness of 88,900 cd m^{−2} with long operating lifetime (T_{50} = 15,850 h at 100 cd m^{−2}).

Online content

Any methods, additional references, Nature Research reporting summaries, source data, extended data, supplementary information, acknowledgements, peer review information; details of author contributions and competing interests; and statements of data and code availability are available at <https://doi.org/10.1038/s41586-020-2791-x>.

- Jang, E., Kim, Y., Won, Y.-H., Jang, H. & Choi, S.-M. Environmentally friendly InP-based quantum dots for efficient wide color gamut displays. *ACS Energy Lett.* **5**, 1316–1327 (2020).
- Shirasaki, Y., Supran, G. J., Bawendi, M. G. & Bulović, V. Emergence of colloidal quantum-dot light-emitting technologies. *Nat. Photon.* **7**, 13–23 (2013).
- Dai, X., Deng, Y., Peng, X. & Jin, Y. Quantum-dot light-emitting diodes for large-area displays: towards the dawn of commercialization. *Adv. Mater.* **29**, 1607022 (2017).
- Colvin, V. L., Schlamp, M. C. & Alivisatos, A. P. Light-emitting diodes made from cadmium selenide nanocrystals and a semiconducting polymer. *Nature* **370**, 354–357 (1994).
- Dai, X. et al. Solution-processed, high-performance light-emitting diodes based on quantum dots. *Nature* **515**, 96–99 (2014).
- Li, X. et al. Quantum-dot light-emitting diodes for outdoor displays with high stability at high brightness. *Adv. Opt. Mater.* **8**, 1901145 (2020).
- Wang, L. et al. Blue quantum dot light-emitting diodes with high electroluminescent efficiency. *ACS Appl. Mater. Interfaces* **9**, 38755–38760 (2017).
- Pu, C. et al. Electrochemically-stable ligands bridge the photoluminescence–electroluminescence gap of quantum dots. *Nat. Commun.* **11**, 937 (2020).
- Yang, Y. et al. High-efficiency light-emitting devices based on quantum dots with tailored nanostructures. *Nat. Photon.* **9**, 259–266 (2015).
- Chen, S. et al. On the degradation mechanisms of quantum-dot light-emitting diodes. *Nat. Commun.* **10**, 765 (2019).
- Won, Y.-H. et al. Highly efficient and stable InP/ZnSe/ZnS quantum dot light-emitting diodes. *Nature* **575**, 634–638 (2019).
- Shen, W. et al. Synthesis of highly fluorescent InP/ZnS small-core/thick-shell tetrahedral-shaped quantum dots for blue light-emitting diodes. *J. Mater. Chem. C* **5**, 8243–8249 (2017).
- Zhang, H. et al. High-brightness blue InP quantum dot-based electroluminescent devices: the role of shell thickness. *J. Phys. Chem. Lett.* **11**, 960–967 (2020).
- Lesnyak, V., Dubavik, A., Plotnikov, A., Gaponik, N. & Eychmüller, A. One-step aqueous synthesis of blue-emitting glutathione-capped ZnSe_{1-x}Te_x alloyed nanocrystals. *Chem. Commun.* **46**, 886–888 (2010).
- Asano, H., Tsukuda, S., Kita, M., Fujimoto, S. & Omata, T. Colloidal Zn(Te,Se)/ZnS core/shell quantum dots exhibiting narrow-band and green photoluminescence. *ACS Omega* **3**, 6703–6709 (2018).
- Jang, E.-P. et al. Synthesis of alloyed ZnSeTe quantum dots as bright, color-pure blue emitters. *ACS Appl. Mater. Interfaces* **11**, 46062–46069 (2019).
- Han, C.-Y. et al. More than 9% efficient ZnSeTe quantum dot-based blue electroluminescent devices. *ACS Energy Lett.* **5**, 1568–1576 (2020).
- Orfield, N. J., McBride, J. R., Keene, J. D., Davis, L. M. & Rosenthal, S. J. Correlation of atomic structure and photoluminescence of the same quantum dot: pinpointing surface and internal defects that inhibit photoluminescence. *ACS Nano* **9**, 831–839 (2015).
- Zhang, L., Lin, Z., Luo, J.-W. & Franceschetti, A. The birth of a type-II nanostructure: carrier localization and optical properties of isoelectronically doped CdSe:Te nanocrystals. *ACS Nano* **6**, 8325–8334 (2012).
- Avidan, A. & Oron, D. Large blue shift of the biexciton state in tellurium doped cdse colloidal quantum dots. *Nano Lett.* **8**, 2384–2387 (2008).
- Brittman, S. et al. Effects of a lead chloride shell on lead sulfide quantum dots. *J. Phys. Chem. Lett.* **10**, 1914–1918 (2019).
- Zherebetsky, D. et al. Hydroxylation of the surface of PbS nanocrystals passivated with oleic acid. *Science* **344**, 1380–1384 (2014).
- Ip, A. H. et al. Hybrid passivated colloidal quantum dot solids. *Nat. Nanotechnol.* **7**, 577–582 (2012).
- Bae, W. K. et al. Highly effective surface passivation of pbse quantum dots through reaction with molecular chlorine. *J. Am. Chem. Soc.* **134**, 20160–20168 (2012).
- Tang, J. et al. Colloidal-quantum-dot photovoltaics using atomic-ligand passivation. *Nat. Mater.* **10**, 765–771 (2011).
- Zhang, H., Jang, J., Liu, W. & Talapin, D. V. Colloidal nanocrystals with inorganic halide, pseudohalide, and halometallate ligands. *ACS Nano* **8**, 7359–7369 (2014).
- Shen, H. et al. High-efficiency, low turn-on voltage blue-violet quantum-dot-based light-emitting diodes. *Nano Lett.* **15**, 1211–1216 (2015).
- Li, X. et al. Bright colloidal quantum dot light-emitting diodes enabled by efficient chlorination. *Nat. Photon.* **12**, 159–164 (2018).
- Takahashi, J. & Naito, H. Visualization of the carrier transport dynamics in layered organic light emitting diodes by modulus spectroscopy. *Org. Electron.* **61**, 10–17 (2018).
- Okachi, T., Nagase, T., Kobayashi, T. & Naito, H. Equivalent circuits of polymer light-emitting diodes with hole-injection layer studied by impedance spectroscopy. *Thin Solid Films* **517**, 1327–1330 (2008).

Publisher's note Springer Nature remains neutral with regard to jurisdictional claims in published maps and institutional affiliations.

© The Author(s), under exclusive licence to Springer Nature Limited 2020

Methods

Materials

Tri-*n*-octylamine (TOA, $\geq 99.0\%$), OA (90%), oleylamine (OAm; technical grade; 70%), diethylzinc (Et_2Zn ; 1.0 M in hexane), zinc acetate ($\text{Zn}(\text{OAc})_2$; 99.99%), zinc chloride (ZnCl_2 ; anhydrous; 99.95%), sulfur (flakes; $\geq 99.99\%$), selenium (granules; 99.99%), tellurium (99.999%), diphenylphosphine (DPP; 98%), HF (48%) and tri-*n*-octylphosphine (TOP; 97%) were purchased from Sigma Aldrich. All other chemicals were also purchased from Sigma Aldrich and used as received unless otherwise noted.

Synthesis of ZnTeSe core

OA (13.5 mmol) and OAm (9 mmol) were mixed with TOA (50 ml) in a four-neck flask by stirring and heated to 120 °C under vacuum. Then, the temperature was further increased to 240 °C under N_2 flow (800 ml min^{-1}). Et_2Zn (9 mmol) was added into the reaction medium, and then a mixture of 2 MSe in TOP (4.5 mmol), 0.1 M Te in TOP (0.3 mmol) and DPP (4.5 mmol) was injected quickly to initiate the reaction. During the injection of Et_2Zn , careful manipulation of the pressure under the N_2 flow was required. After 40 min, the ZnTeSe cores were isolated by centrifugation using ethanol and were dispersed in hexane.

Synthesis of ZnTeSe/ZnSe/ZnS QDs

$\text{Zn}(\text{OAc})_2$ (4.8 mmol) and OA (9.6 mmol) were mixed with TOA (80 ml) solvent in a four-neck flask by stirring, and the mixture was heated to 120 °C under vacuum and kept at that temperature for 15 min. After the atmosphere was changed to N_2 , the mixed solution was heated to 280 °C to prepare the $\text{Zn}(\text{OA})_2$ precursor, and then cooled to 240 °C. The ZnTeSe core (optical density of 0.54 at 383 nm, 8 ml) was quickly injected into the $\text{Zn}(\text{OA})_2$ precursor. Diluted HF (10 wt%, 0.44 ml) and ZnCl_2 (0.09 mmol) in acetone were added to the reaction mixture, and the temperature was increased to 340 °C. During the addition of dilute HF and ZnCl_2 in acetone, careful manipulation of the pressure under N_2 flow was required. For ZnSe mid-shell growth, 18 mmol of $\text{Zn}(\text{OA})_2$ in TOA and 2 M TOP-Se (12.0 mmol) were added at 340 °C and reacted for 1 h. For ZnS shell growth, 9.6 mmol of $\text{Zn}(\text{OA})_2$ in TOA and 22.4 mmol of 1 M TOP-S were added and further reacted for 1.5 h. We balanced the precursor concentrations to control the reaction rates for the growth of the core and of each shell, and maintained the metal precursor in excess of the stoichiometric ratio during the reaction. The resulting ZnTeSe/ZnSe/ZnS C/S/S QDs were isolated by centrifugation using ethanol and dispersed in hexane.

Ligand exchange in the liquid phase

The as-synthesized C/S/S QDs (optical density of 0.25 at 420 nm, 6 ml) were separated by centrifugation using ethanol and re-dispersed in 6 ml cyclohexane. 0.022 mmol of ZnCl_2 (7.3 M ZnCl_2 in ethanol solution) was added to the C/S/S QD solution. The mixture was heated to 80 °C and maintained for 30 min. Then, the QDs (C/S/S-Cl(I)) were separated by centrifuging twice and were re-dispersed in octane. All processes were carried out in a N_2 -filled glove box.

Material characterization

The absorption and photoluminescence spectra of the QDs were measured with a ultraviolet–visible spectrometer (Varian Cary 5000) and a fluorescence spectrophotometer (Hitachi F7000), respectively. The photoluminescence quantum yield was determined using a QE-2100 integrating hemisphere (Otsuka). TR-PL spectra were obtained with a FluoTime 300 fluorescence lifetime spectrometer (PicoQuant). TEM analysis was performed on a Titan ChemiSTEM electron microscope operated at 200 keV. Scanning electron microscopy (SEM) images were obtained using a Hitachi S-4700 system with an accelerating voltage of 5.0 kV. XPS measurements were carried out using a Quantera II system equipped with a mono-chromatized Al K α source. XRD patterns were

recorded by a D8 Advance (Bruker) instrument using a Cu K α source. TGA was performed from 20 °C to 600 °C at a heating rate of 10 °C min^{-1} under N_2 using a Trios V3.2 system (TA Instruments). FT-IR data were measured by a Varian 670-IR spectrometer with an ATR hemisphere. The hydrodynamic particle sizes of the QDs in solutions were determined using a particle-size analyser (ELSZ-2000, Otsuka). The ionization potential was measured by a photoelectron spectrophotometer (AC3, Riken Keiki) in air.

Device fabrication and characterization

Patterned indium tin oxide (ITO) glass (Techno Print Co. Ltd; sheet resistance $\sim 10 \Omega$ per square, thickness 150 nm) was cleaned with acetone and isopropanol (IPA) in an ultrasonic bath and then dried. Oxygen plasma treatment was applied for 20 min using a ultraviolet ozone cleaner (Jelight, UVO144AX-220). A 70:30 (per volume) mixture of poly(ethylenedioxythiophene):polystyrene sulfonate (PEDOT:PSS; Heraeus Clevios, AI 4083) and IPA was spin-coated on the ITO glass at 2,200 rpm for 50 s, followed by baking at 150 °C for 10 min in air and then baking at 150 °C for 30 min in a N_2 -filled glove box. A 0.7 wt% solution of poly(9,9-dioctyl-fluorene-co-N-(4-(3-methylpropyl))diphenylamine (TFB; Sumitomo Chemical; molecular weight of $\sim 300,000$) dissolved in oxylene was spin-coated over the PEDOT:PSS layer at 2,000 rpm for 40 s, followed by baking at 150 °C for 30 min in a N_2 -atmosphere glove box. The QD EML (28 nm/13 nm) over the TFB layer was prepared as follows. C/S/S-Cl(I) in octane (15 mg ml^{-1}) was spin-coated at 3,000 rpm for 10 s, and the film was baked at 80 °C for 20 min under N_2 . Then, 0.7 M ZnCl_2 in ethanol was drop-casted on the bottom QD layer and kept there for 60 s, and then the film was spun at 1,000 rpm for 40 s. To remove extra ZnCl_2 , two consecutive rinsing steps with neat ethanol were carried out by spin-coating, and the film was baked at 80 °C for 20 min. To make the top EML, C/S/S-Cl(I) in octane (15 mg ml^{-1}) was spin-coated over the bottom layer at 3,000 rpm for 10 s. A solution of ZnMgO nanoparticles (12 mol% Mg, 70 mg ml^{-1} in ethanol), prepared according to a previous reported method³¹, was spin-coated at 4,000 rpm for 10 s and annealed at 80 °C for 30 min under N_2 . The thicknesses of the QD layers and the ZnMgO layer were controlled by the spin speed. An aluminium cathode was deposited by a thermal evaporator at a rate of 1 \AA s^{-1} under vacuum ($< 5 \times 10^{-7}$ torr), and then the device was encapsulated in cover glass. The EOD was prepared with the structure ITO (150 nm)/ZnMgO (20 nm)/QD/ZnMgO (20 nm)/Al (100 nm) via spin coating. The HOD was prepared with the structure ITO (150 nm)/PEDOT:PSS (30 nm)/TFB (25 nm)/QD/TCTA (36 nm)/HATCN (10 nm)/Ag (100 nm). All layers were processed according to the method described above, except for tris(4-carbazoyl-9-ylphenyl)amine (TCTA) and 1,4,5,8,9,11-hexa-a zatriphenylene hexacarboxitrile (HATCN), which were deposited by thermal evaporation. The device performance was determined using a CS-2000A spectroradiometer (Minolta) and a source meter (Keithley 2635B). The lifetimes of the QD-LEDs were measured by an in-house setup with a multi-channel system consisting of an embedded photodiode in a temperature/humidity-controlled chamber (23 °C, 45%). The electrochemical impedance spectra of the device were measured using an SP-300 impedance analyser (Biologic).

Modelling

The computations were carried out using the pseudo-potential DFT method with a plane-wave basis set³². The exchange correlation of electrons was treated within the generalized gradient approximation of Perdew–Burke–Ernzerhof³³. The cut-off energy for the expansion of wave functions and potentials in the plane-wave basis was chosen to be 400 eV. We used the projector-augmented wave pseudo-potentials of the Vienna ab initio simulation package³⁴. Brillouin zone sampling for the (100) Zn surface with 15 Å slab thickness was performed with $3 \times 3 \times 1$ and $5 \times 5 \times 1$ grids for the ionic relaxation and the DOS calculation, respectively. For bandgap corrections, we used the Heyd–Scuseria–Ernzerhof hybrid functional³⁵ for the DOS calculations.

Atomic relaxation was carried out until the Hellmann–Feynman forces were less than 0.02 eV \AA^{-1} . The vacuum layer in the supercell was set as 15 \AA to minimize the artificial interlayer interaction. The ligand binding energy was estimated as $E_{\text{Binding}} = E_{(\text{ZnS-ligand})} - (E_{\text{ZnS}} + \mu_{\text{ligand}})$, where $E_{(\text{ZnS-ligand})}$ and E_{ZnS} are the total energy of the passivated and bare slab, respectively, and μ_{ligand} is the chemical potential of the ligand. The chemical potentials of Cl, Zn and acetate were referenced from Cl_2 (gas) ($3.575 \text{ eV per Cl}_2$) and zinc acetate ($87.79 \text{ eV per zinc acetate}$). The binding energy was calculated in a Zn-rich environment at $\mu_{\text{Zn}} = \mu_{\text{Zn(bulk)}}$ (1.10 eV per Zn).

Effective-mass approximation calculation

The emission wavelengths of $\text{ZnTe}_x\text{Se}_{1-x}/\text{ZnSe}/\text{ZnS}$ ($x = 0, 0.033$ and 0.067) QDs were calculated with effective-mass approximation. The electron effective masses of ZnTe, ZnSe and ZnS used in the calculation were $0.09, 0.16$ and 0.39 , and the hole effective masses were $0.6, 0.75$ and 1.76 ; the corresponding relative permittivities were $10.3, 9.1$ and 8.9 (ref. ³⁶). The overall effective mass and relative permittivity of the $\text{ZnTe}_x\text{Se}_{1-x}$ core is averaged by the mole fraction of the elemental components, and the bulk energy bandgap is derived as $E_g = 2.72 - 1.837x + 1.450x^2$ (ref. ³⁶). The bulk energy bandgap of ZnS is 3.68 eV (ref. ³⁷). The valence band offset between $\text{ZnTe}_x\text{Se}_{1-x}$ and ZnS for $x = 1/30$ and $x = 1/15$ is 0.06 and 0.12 eV , respectively³⁸, and the offset between ZnSe and ZnS is 0.52 eV (ref. ³⁹).

Data availability

All data generated or analysed during this study are included in the paper and its Supplementary Information files.

31. Qian, L., Zheng, Y., Xue, J. & Holloway, P. H. Stable and efficient quantum-dot light-emitting diodes based on solution-processed multilayer structures. *Nat. Photon.* **5**, 543–548 (2011).
32. Cohen, M. L. Pseudopotentials and total energy calculations. *Phys. Scr.* **T1**, 5–10 (1982).
33. Perdew, J. P., Burke, K. & Ernzerhof, M. Generalized gradient approximation made simple. *Phys. Rev. Lett.* **77**, 3865–3868 (1996).
34. Kresse, G. & Hafner, J. Ab initio molecular-dynamics simulation of the liquid-metal–amorphous-semiconductor transition in germanium. *Phys. Rev. B* **49**, 14251–14269 (1994).
35. Heyd, J., Scuseria, G. E. & Ernzerhof, M. Hybrid functionals based on a screened Coulomb potential. *J. Chem. Phys.* **118**, 8207–8215 (2003).
36. Kim, S. et al. Efficient blue-light-emitting Cd-free colloidal quantum well and its application in electroluminescent devices. *Chem. Mater.* **32**, 5200–5207 (2020).

37. Asano, H. & Omata, T. Design of cadmium-free colloidal II–VI semiconductor quantum dots exhibiting RGB emission. *AIP Adv.* **7**, 045309 (2017).
38. Faschinger, W., Ferreira, S. & Sitter, H. Doping of zinc-selenide-telluride. *Appl. Phys. Lett.* **64**, 2682–2684 (1994).
39. Li, Y.-H. et al. Revised ab initio natural band offsets of all group IV, II–VI, and III–V semiconductors. *Appl. Phys. Lett.* **94**, 212109 (2009).
40. Kwak, J. et al. Bright and efficient full-color colloidal quantum dot light-emitting diodes using an inverted device structure. *Nano Lett.* **12**, 2362–2366 (2012).
41. Lee, K.-H. et al. Highly efficient, color-pure, color-stable blue quantum dot light-emitting devices. *ACS Nano* **7**, 7295–7302 (2013).
42. Shen, H. et al. Efficient and long-lifetime full-color light-emitting diodes using high luminescence quantum yield thick-shell quantum dots. *Nanoscale* **9**, 13583–13591 (2017).
43. Lin, Q. et al. Nonblinking quantum-dot-based blue light-emitting diodes with high efficiency and a balanced charge-injection process. *ACS Photonics* **5**, 939–946 (2018).
44. Wang, O. et al. High-efficiency, deep blue $\text{ZnCdS}/\text{Cd}_{1-x}\text{Zn}_x\text{S}/\text{ZnS}$ quantum-dot-light-emitting devices with an EQE exceeding 18%. *Nanoscale* **10**, 5650–5657 (2018).
45. Shen, H. et al. Visible quantum dot light-emitting diodes with simultaneous high brightness and efficiency. *Nat. Photon.* **13**, 192–197 (2019).
46. Shen, H. et al. Phosphine-free synthesis of high quality ZnSe, ZnSe/ZnS, and Cu-, Mn-doped ZnSe nanocrystals. *Dalt. Trans.* **47**, 10534–10540 (2009).
47. Ji, W. et al. High color purity ZnSe/ZnS core/shell quantum dot based blue light emitting diodes with an inverted device structure. *Appl. Phys. Lett.* **103**, 053106 (2013).
48. Ippen, C. et al. ZnSe/ZnS quantum dots as emitting material in blue QD-LEDs with narrow emission peak and wavelength tunability. *Org. Electron.* **15**, 126–131 (2014).
49. Lin, Q. et al. Cadmium-free quantum dots based violet light-emitting diodes: high-efficiency and brightness via optimization of organic hole transport layers. *Org. Electron.* **25**, 178–183 (2015).
50. Wang, A. et al. Bright, efficient, and color-stable violet ZnSe-based quantum dot light-emitting diodes. *Nanoscale* **7**, 2951–2959 (2015).
51. Ji, B., Koley, S., Slobodkin, I., Remennik, S. & Banin, U. ZnSe/ZnS core/shell quantum dots with superior optical properties through thermodynamic shell growth. *Nano Lett.* **20**, 2387–2395 (2020).

Acknowledgements We thank H. Kim in RIAM of SNU for the TEM analysis and H. Jung for the photospectroscopic measurements.

Author contributions The synthesis and structural analysis of QDs were performed by T.K., H.J. and S.K. The chloride exchange and analysis were performed by T.K. and K.-H.K. The QD-LEDs were fabricated and characterized by K.-H.K., H.-K.S., H.L., D.-Y.C. and T.K. The modelling was performed by S.-M.C. This research was designed and coordinated by E.J. The manuscript was written by T.K. and E.J. in consultation with all authors.

Competing interests The authors declare no competing interests.

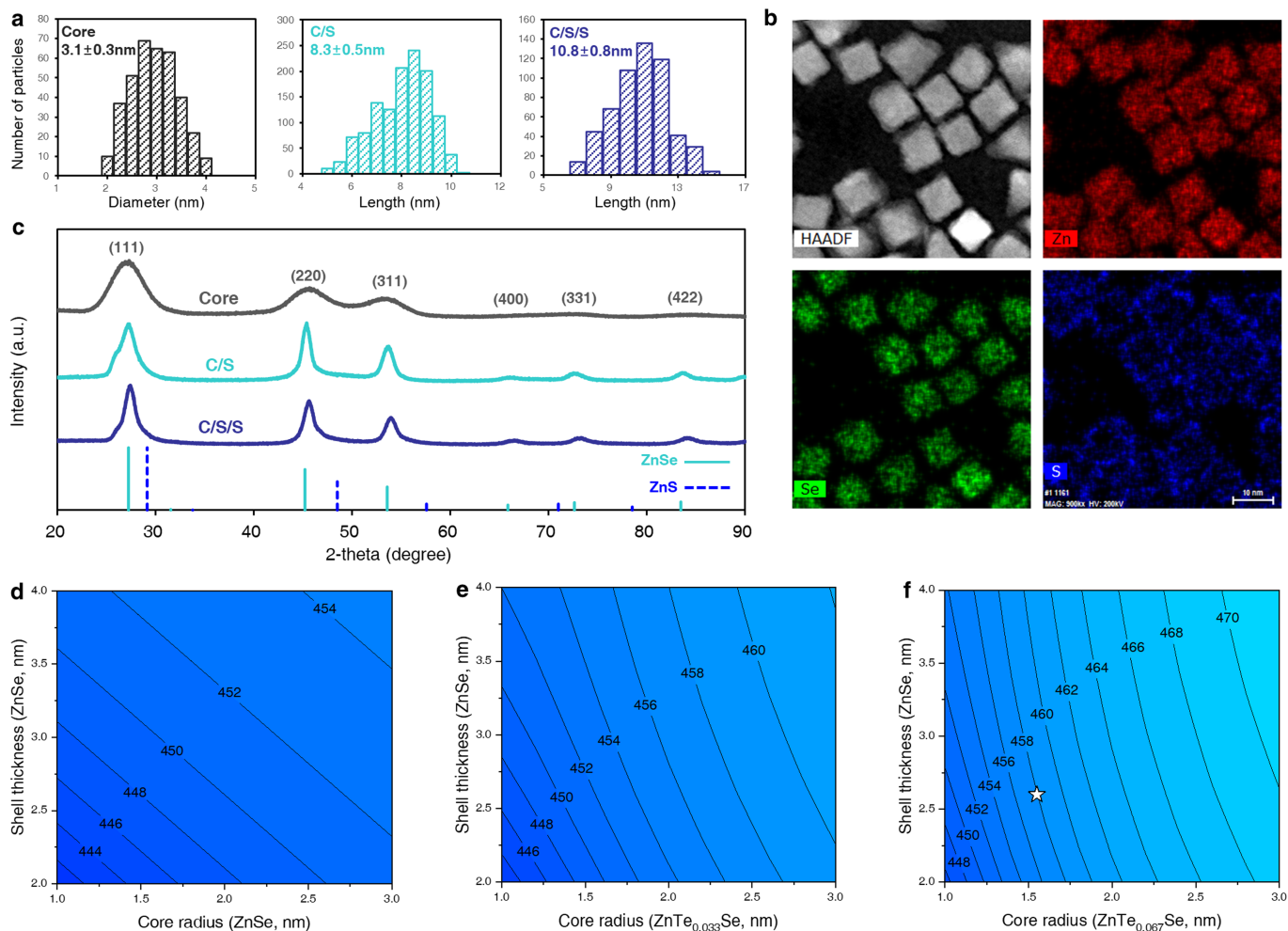
Additional information

Correspondence and requests for materials should be addressed to E.J.

Peer review information Nature thanks the anonymous reviewers for their contribution to the peer review of this work. Peer reviewer reports are available.

Reprints and permissions information is available at <http://www.nature.com/reprints>.

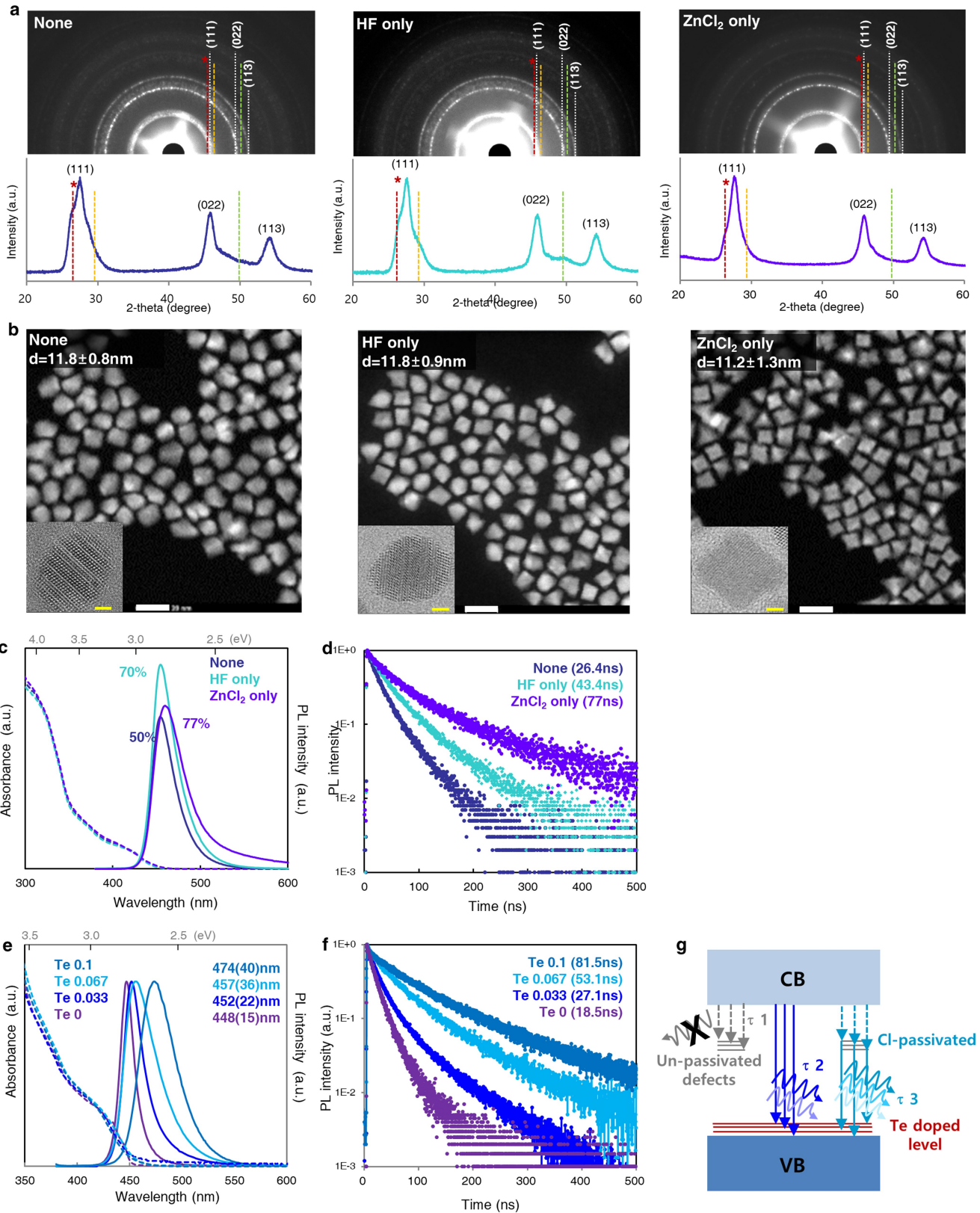
Article



Extended Data Fig. 1 | Characterization of core, C/S and C/S/S QDs.

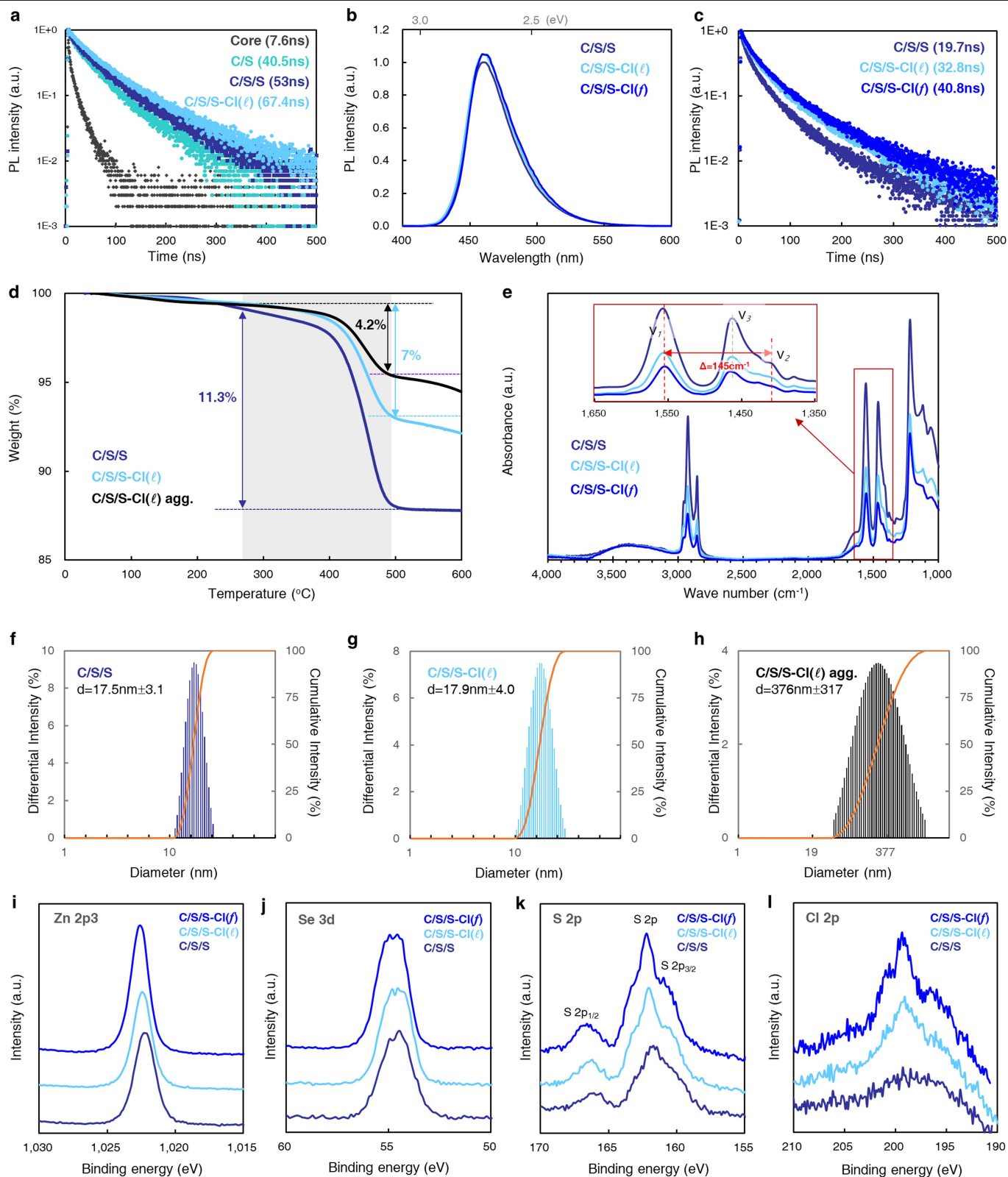
a, Particle-size distributions of core, C/S and C/S/S QDs, determined from the respective STEM images in Fig. 1. **b**, Elemental mapping of C/S/S QDs obtained by STEM-EDX. **c**, XRD patterns of core, C/S and C/S/S QDs, together with the reference zinc blende structure of ZnSe (X-ray diffraction pattern PDF

00-037-1463) and ZnS (PDF 00-005-0566). **d-f**, Contour maps of the calculated emission wavelength of ZnTe_x/ZnSe/ZnS (with a fixed ZnS thickness of 1.2 nm) as a function of ZnTe_xSe_{1-x} core size and ZnSe shell thickness for $x = 0$ (**d**), $x = 0.033$ (**e**) and $x = 0.067$ (**f**). The star in **f** corresponds to the C/S QD shown in Fig. 1.



Extended Data Fig. 2 | Effect of HF and ZnCl₂ additives on structure and optical properties. **a**, SAED and XRD patterns of ZnTeSe/ZnSe/ZnS C/S/S QDs prepared without any additives (left), with HF only (middle) and with ZnCl₂ only (right). The red, yellow and green dashed lines indicate stacking faults assigned to 26°, 29° and 50°, respectively. **b**, STEM images (white scale bar, 20 nm). Inset, high-resolution TEM images (yellow scale bar, 2 nm). **c**, **d**, Absorption and photoluminescence spectra (**c**) and TR-PL profiles (**d**) of ZnTeSe/ZnSe/ZnS

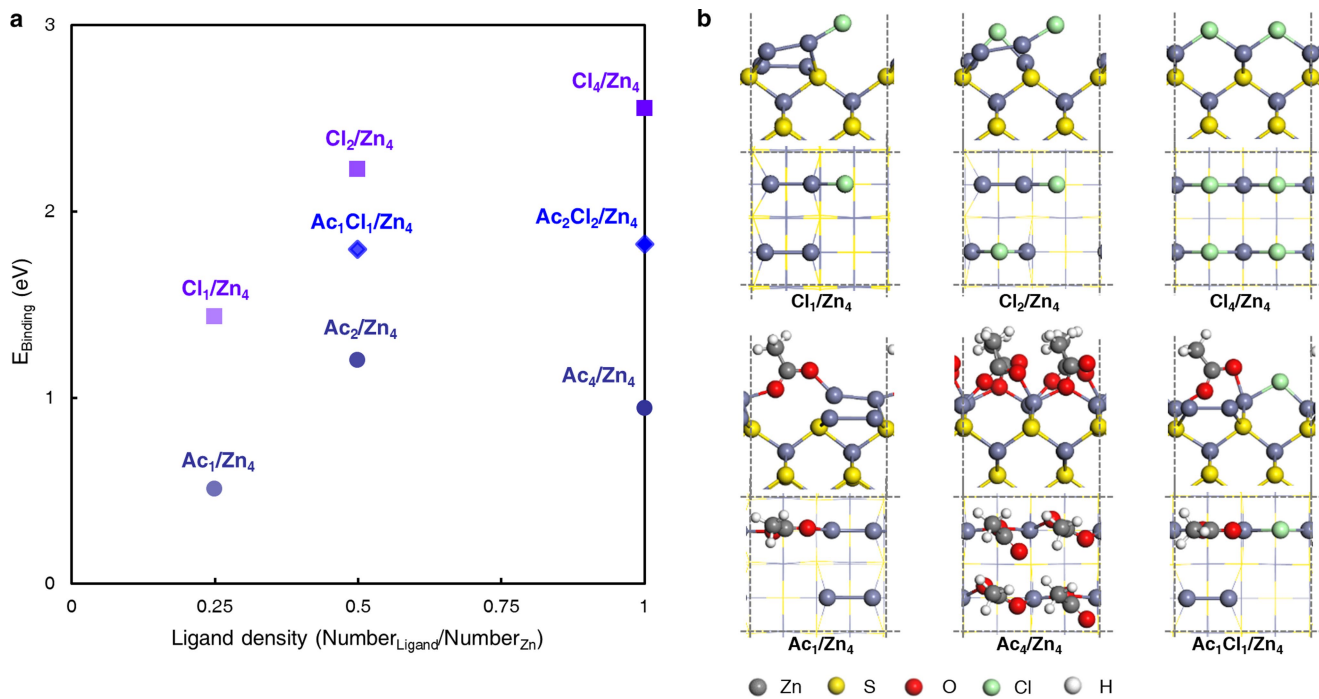
C/S/S QDs prepared without any additive ('None'), with HF only and with ZnCl₂ only. Average decay lifetimes fitted with a multi-component exponential function are indicated. **e**, **f**, Absorption and photoluminescence spectra (**e**) and TR-PL profiles (**f**) of ZnTe_xSe_{1-x}/ZnSe/ZnS C/S/S QDs with $x = 0, 0.033, 0.067$ and 0.1 . **g**, Schematic energy level diagram of radiative and non-radiative transition pathways. CB, conduction band; VB, valence band.



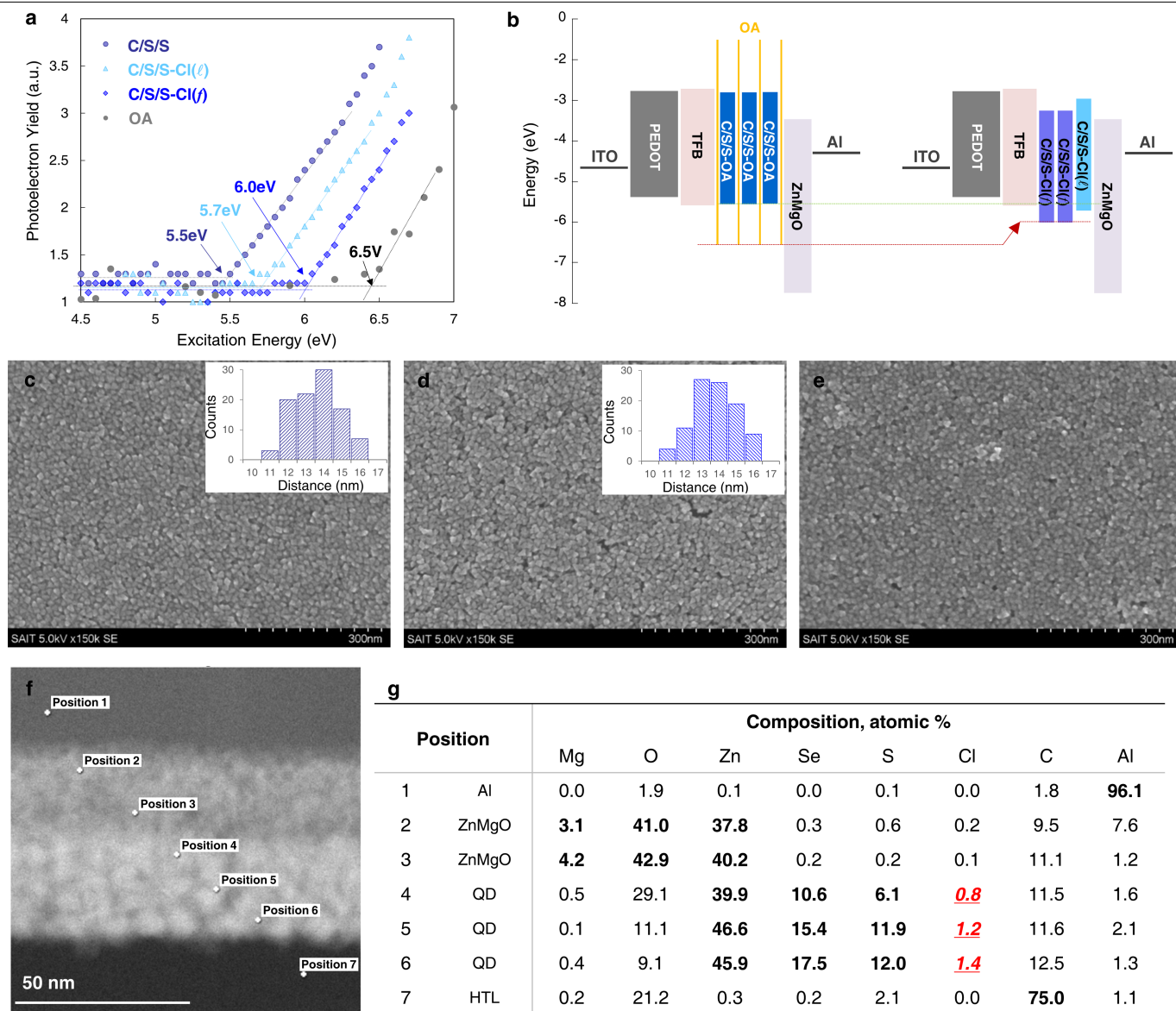
Extended Data Fig. 3 | Effect of chloride passivation on physical properties.

a, TR-PL spectra and average decay lifetimes of solutions of core, C/S, C/S/S and C/S/S-Cl(I) QDs (excitation at 405 nm, measured at each emission peak). **b**, **c**, Photoluminescence spectra (**b**) and TR-PL spectra and average decay lifetimes (**c**) of films of C/S/S, C/S/S-Cl(I) and C/S/S-Cl(f) QDs. **d**, TGA curves of C/S/S, C/S/S-Cl(I) and C/S/S-Cl(I) aggregates. The shaded area indicates the weight loss of OA ligands. **e**, FT-IR spectra of films prepared with C/S/S, C/S/S-Cl(I) and C/S/S-Cl(f) QDs. Inset, magnification of the spectra showing

asymmetric (ν₁) and symmetric (ν₂) vibrations of the carboxylate group with aliphatic stretching (ν₃). The wavenumber difference between ν₁ and ν₂ is indicated (145 cm⁻¹) to explain the binding mode of oleate corresponding to bridging bidentate. **f**–**h**, Size of QDs dispersed in octane and measured with DLS: C/S/S (**f**), C/S/S-Cl(I) (**g**) and C/S/S-Cl(I) (**h**) aggregates. **i**–**l**, High-resolution XPS spectra of elements in C/S/S, C/S/S-Cl(I) and C/S/S-Cl(f): zinc 2p_{3/2} (**i**), selenium 3d (**j**), sulfur 2p (**k**) and chlorine 2p (**l**).



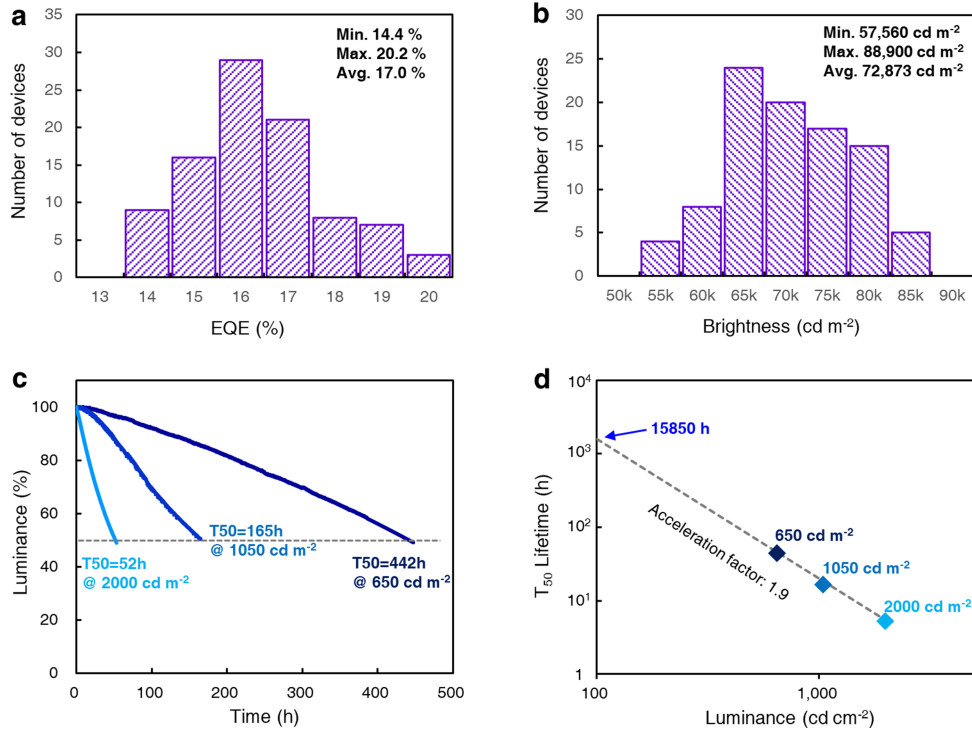
Extended Data Fig. 4 | Dependence of ligand binding energy on ZnS surface. **a**, Calculated binding energy of Ac and Cl with Zn atoms on a ZnS (100) surface as a function of ligand density. **b**, Optimized structures of Ac and Cl on ZnS(100) surfaces for each composition.



Extended Data Fig. 5 | Analysis of chlorinated films and resulting devices.

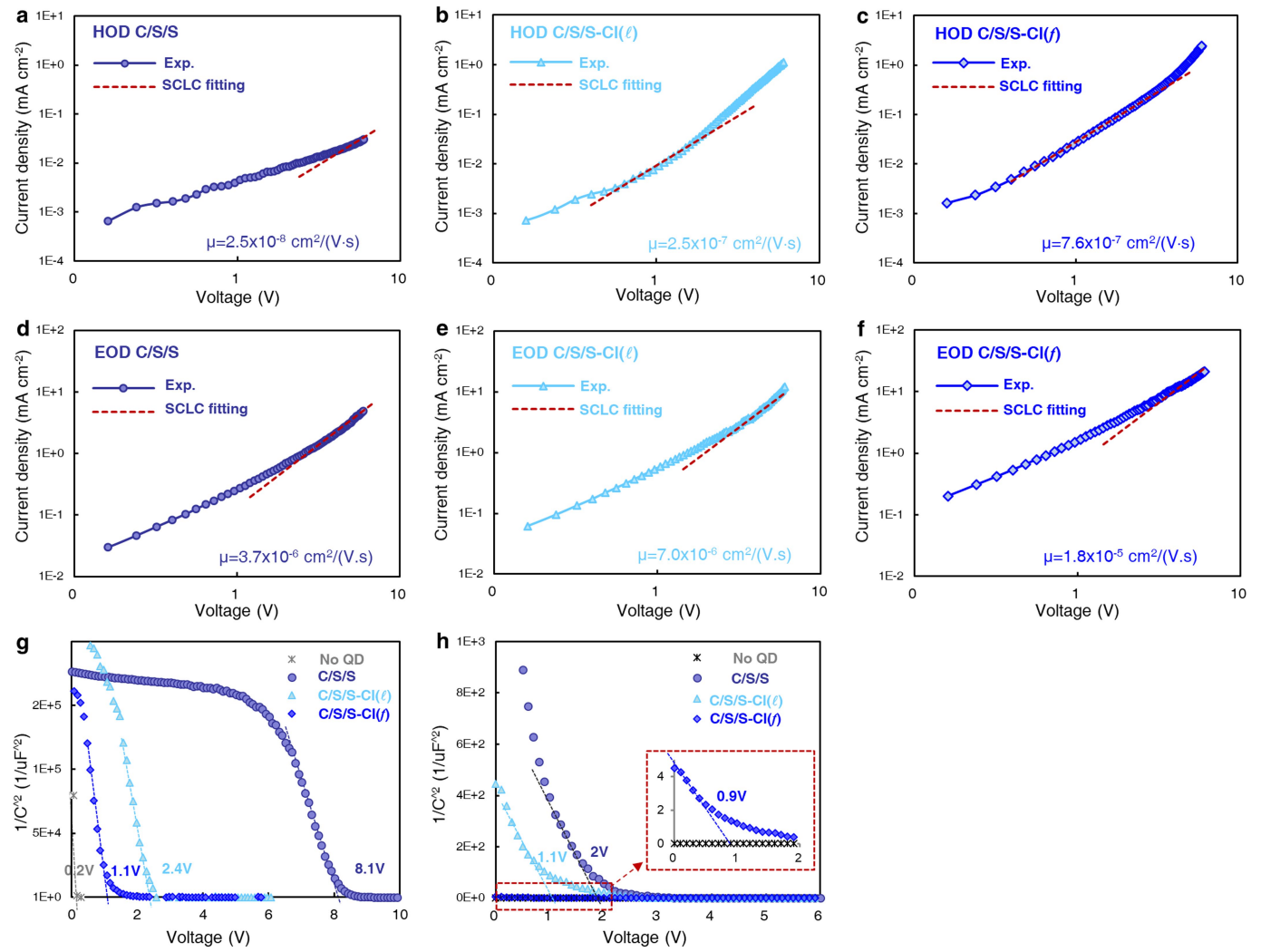
a, Photoelectron spectroscopy data for C/S/S, C/S/S-Cl(l), C/S/S-Cl(f) and OA films. The corresponding ionization potentials are indicated. **b**, Energy-band diagrams of QD-LEDs with C/S/S-OA (left) and double EMLs (right). **c–e**, SEM images of QD films prepared with C/S/S (**c**), C/S/S-Cl(f) (**d**) and a double layer consisting of C/S/S-Cl(f) (bottom layer) and C/S/S-Cl(l) (top layer) (**e**).

Insets, dot-to-dot distances between QDs for C/S/S and C/S/S-Cl(f) (the average distances are 14.1 ± 1.2 nm and 13.7 ± 1.2 nm, respectively). **f**, Cross-sectional TEM image used for EDX elemental analysis of the QD-LED with a double EML of C/S/S-Cl(l) over C/S/S-Cl(f). **g**, Elemental composition at each probed position in **e**.



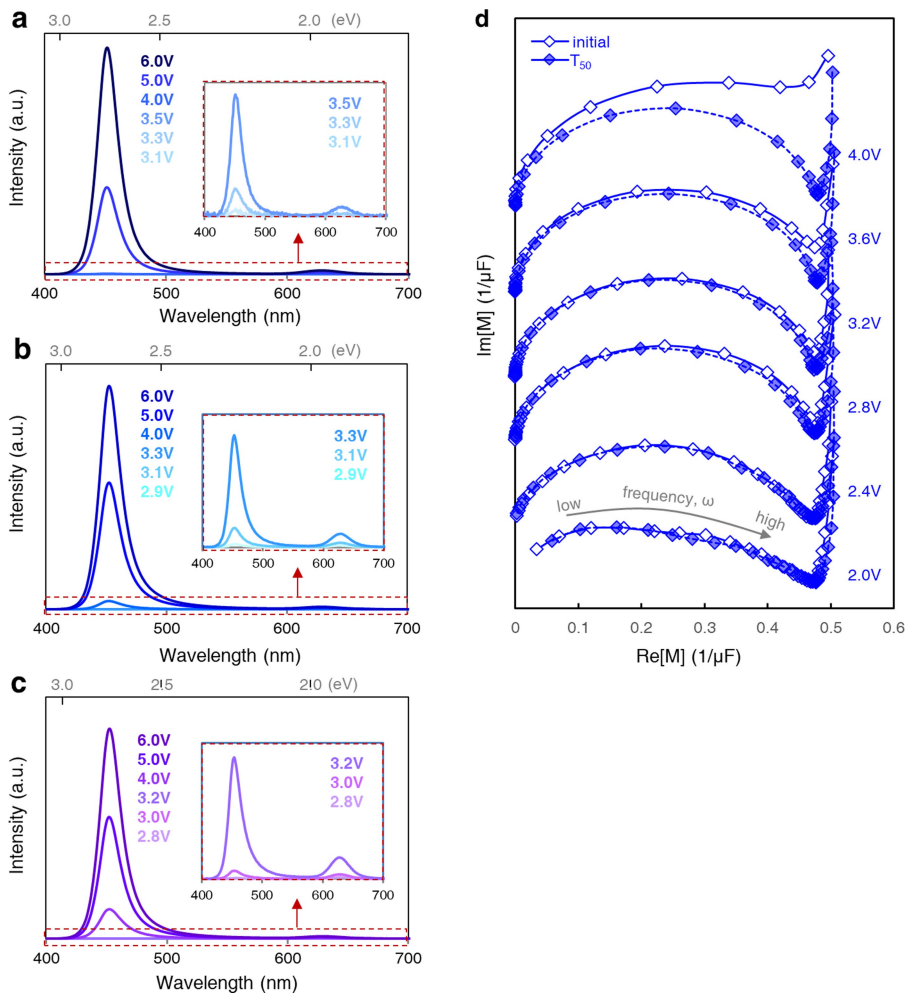
Extended Data Fig. 6 | Statistics of device performance. **a, b**, Distributions of maximum EQE (**a**) and maximum brightness (**b**) obtained from 90 QD-LEDs with double EML. **c**, Operational lifetimes of QD-LEDs with a double EML consisting of C/S/S-Cl(l) over C/S/S-Cl(f) for different initial brightness values. **d**, Measured

lifetime (T_{50}) of the devices versus brightness. The T_{50} value at 100 cd m^{-2} was estimated by fitting with the empirical equation $L_0^n \times T_{50} = \text{constant}$, where L_0 is the initial brightness and n is the acceleration factor.



Extended Data Fig. 7 | Characterization of single-carrier devices. **a–f**, Current density–voltage characteristics and mobilities calculated from the fitting curves using the space charge-limited current model (SCLC) for HODs with C/S/S,

C/S/S-CI(ℓ) and C/S/S-CI(f) QDs (**a–c**) and EODs with C/S/S, C/S/S-CI(ℓ) and C/S/S-CI(f) QDs (**d–f**). **g, h**, Mott–Schottky analysis of HODs (**g**) and EODs (**h**) with no QDs and with C/S/S, C/S/S-CI(ℓ) and C/S/S-CI(f) QDs.



Extended Data Fig. 8 | Analysis of double-EML devices. **a–c**, Voltage-dependent electroluminescence spectra of QD-LEDs with double EML, consisting of a C/S/S top layer with red-emitting InP/ZnSe/ZnS QDs and different bottom EMLs: C/S/S (**a**), C/S/S-Cl(l) (**b**) and C/S/S-Cl(f) (**c**). The insets show electroluminescence spectra at low voltages. **d**, Complex modulus spectra measured at various

voltages before and after the T_{50} lifetime test for QD-LEDs with C/S/S-Cl(f). The real (horizontal axis) and imaginary (vertical axis) moduli were calculated using the equation $M = i\omega Z$, where i is the imaginary unit, ω is the frequency and Z is the complex impedance²⁹. The grey arrow shows the direction of increasing frequency.

Extended Data Table 1 | Quantitative analysis of surface ligands

	C/S/S	C/S/S-Cl(<i>l</i>)	C/S/S-Cl(<i>f</i>)
QD size (length, nm) <i>measured from TEM</i>	10.8		
Surface area of QD (nm ²) <i>assuming cube</i>	699.8		
Molecular weight of QD <i>ZnSe, ZnTe volume calculated from TEM</i>	2,010,764		
Total number of Zn in QD <i>(100) unit cell area = 0.29</i>	16,268		
Number of Zn atoms on surfaces / QD <i>Number of Zn in unit cell = 2</i>	4,765		
Ligand (wt%) <i>Measured from TGA</i>	11.3	7	-
Relative OA concentration <i>measured from FT-IR</i>	1	0.65	0.3
Number of OA ligands / QD	907	562	272
Bound Zn surface with OA (%) <i>Assuming bidentate coordination</i>	38%	24%	11%
Cl/Zn mole ratio <i>measured from XPS</i>	0.01	0.10	0.18
Number of Cl atoms / QD	163	1,611	2,847
Bound Zn surface with Cl (%) <i>Assuming bidentate coordination</i>	-	68%	119%
Total bound Zn surface (%) <i>Assuming bidentate coordination</i>	38%	91%	131%

In the calculations, we assumed that a QD has a cubic shape with (100) facets and that all the outer atoms on the surface are Zn atoms. The number of OA ligands per QD particle was calculated using the weight loss from TGA (Extended Data Fig. 3d) and the relative intensity changes at 1,545 cm⁻¹ in the FT-IR analysis (Extended Data Fig. 3e). The number of Cl atoms was calculated based on the elemental ratio obtained from the XPS analysis (Extended Data Fig. 3i-l). According to our DFT modelling, the Zn atoms are assumed to coordinate with OA or Cl in bidentate mode (Fig. 2c).

Extended Data Table 2 | Comparison of state-of-the-art blue QDs and blue QD-LEDs reported in the literature with those described here

Structure	QD (PL)				QD-LED (EL)				Literature	Ref.	
	Wavelength (nm)	FWHM (nm)	PLQY (%)	EQE (%)	Brightness (cd m ⁻²)	Wavelength (nm)	FWHM (nm)	T _{50, re-calculate} (h@100 cd m ⁻²)			Lifetime (As reported)
CdZnS	433			1.7	2,250	437				Nano Lett. 12, 2362 (2012)	40
CdZnS	452		98	7.1	2,624	452	31			ACS Nano. 7, 7295 (2013)	41
CdZnS				10.7	4,000	455	20	1,000		Nat. Photonics. 9, 259 (2015)	9
CdSe	466		87	19.8	4,890	468	20	16	T50=0.5h (1,008 cd m ⁻²)	ACS Appl. Mater. Interfaces. 9, 38755 (2017)	7
CdZnS	442		93	15.6	4,500	445	25	566	T70=47h (420 cd m ⁻²)	Nanoscale. 9, 13583 (2017)	42
CdZnSe	454			13.2	20,900	462	30	355		ACS Photonics. 5, 939 (2018)	43
CdZnS	441	15	100	18	6,768	445	19	47.4		Nanoscale. 10, 5650 (2018)	44
CdZnSeS				12.5	2,500	467		727	T50=23h (1,000 cd m ⁻²)	Nat. Commun. 10, 765 (2019)	10
CdZnSe			73	8.1	62,600	477		7,000		Nat. Photonics. 13, 192 (2019)	45
CdSeS				10		480		10,000		Nat. Commun. 11, 937(2020)	8
InP	477	44	76		90	488	45			J. Mater. Chem. C. 5, 8243 (2017)	12
InP	480	45	81	1.01	3,120	488	50	2		J. Phys. Chem. Lett 11, 960 (2020)	13
ZnSe	414~425	14~17	70							Dalt. Trans., 10534 (2009)	46
ZnSe	390~460	21~30	45							Chem. Commun. 46, 7331 (2010)	14
ZnSe	439	11	60	1.5 (0.5cd/A)	1,170	441	15			Appl. Phys. Lett. 103, 053106 (2013)	47
ZnSe	435	16	40			435				Org. Electron. 15, 126 (2014)	48
ZnSe	425		80	7.4	2,856	429	21			Org. Electron. 25, 178 (2015)	49
ZnSe	440~455	12~20	83	7.83	2,632	429	20			Nanoscale. 7, 2951 (2015)	50
ZnTeSe	441	32	70	4.2	1,195	445		0.24	T50=5min (200 cd m ⁻²)	ACS Appl. Mater. Interfaces. 11, 46062 (2019)	16
ZnTeSe	445	27	84	9.5	2,904	445				ACS Energy Lett. 5, 1568 (2020)	17
ZnSe	430	18	85							Nano Lett. 20, 2387 (2020)	51
ZnTeSe	457	36	100	20.2	88,900	460	35	15,850		This work	

Previous data from refs. ^{7-10,12-14,16,17,40-51}